Whitening Filters Application for Ionospheric Propagation Delay Extraction

Lubos Rejfek, Karel Juryca, *Member, IEEE*, Tan N. Nguyen, *Member, IEEE*, Ladislav Beran, and Miroslav Voznak, *Senior Member, IEEE*

***Abstract*— Preprocessed signals from Global Positioning System (GPS) satellites can be used for ionospheric research. Important ionospheric characteristics are for example ionospheric propagation delays and scintillations. These characteristics are important for understanding the ionosphere and showing how the ionosphere reacts to external forces (e.g., geomagnetic disturbance, solar eclipse, etc.). Dual-frequency systems use an approach based on the difference between two pseudoranges. However, this approach has two possible disadvantages: 1) the price of the dual frequency receiver is relatively high and 2) both pseudoranges can affect the obtained results so the operators cannot separately analyze their relative contribution. The objective of the article is to demonstrate an algorithm for processing data from a GPS receiver. The algorithm does not merge the pseudoranges obtained from different carrier waves. Accordingly, it was decided to use whitening filters to accomplish this task for every frequency separately. Compared with the dual-frequency approach, the obtained results of the newly developed algorithm demonstrate that this algorithm works accurately, and the propagation delays can be estimated independently of the used frequency.**

***Index Terms*— Global Positioning System (GPS), ionospheric delay, pseudorange, signal propagation, whitening filter.**

I. Introduction

IONOSPHERIC measurements are essential for electronic systems because the presence of free-charged particles in the ionosphere affects the precision of communication and navigation systems. If the frequency of the propagating signal is lower than the plasma frequency, the transmitted signals are reflected [1]. The plasma frequency is calculated according to the following equation; see [2]:

$$f_N^2 = \frac{N_e \cdot e^2}{\varepsilon_0 \cdot m} \tag{1}$$

where N_e represents the electron concentration, e represents the electron charge, m is the mass of the electrons, and ε_0 is the permittivity of the vacuum.

The signal's propagation delay due to the ionosphere has significant consequences for the Global Navigation Satellite System (GNSS). Because the signal influences to be removed by our approach are caused by the GNSS system parameters (time bias and others), the algorithm is valid for all the ionospheric conditions.

Ionospheric radars can be based on the pulse [4] or the FMCW system [7]. Nowadays, the pulse ionosonde systems are used for the vertical and oblique sounding and measurement of traveling ionospheric disturbances (TID), as described in [5] and [6]. An example of the ionospheric profiles of the plasma frequency, measured for 15 h, is shown in Fig. 1. The shape of the profile is dependent on the time of day, season, solar and geomagnetic activity, and other sources. Another type of ionospheric measurement can be realized with the continuous Doppler sounding system (CDSS), which is described in [8] and [9]. The third possible way to monitor the state of the ionosphere is based on GNSS, one of which is the Global Positioning System (GPS). The application of the GPS for ionospheric measurements is presented in [10]. Vertical total electron content (VTEC) can be obtained from the GNSS signals during the post-processing. The slant TEC (STEC) is the integral of free electrons in a column (defined as unit cross-sectional area) between the satellite and the GNSS receiver [11]. The TEC influences the delay of the

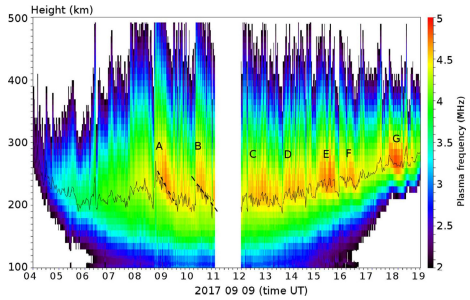

Fig. 1. Example of the electron density profiles during part of one day measured at the observatory Průhonice [3].

Manuscript received 19 February 2023; revised 24 April 2023; accepted 1 May 2023. Date of publication 24 May 2023; date of current version 9 June 2023. This work was supported by the European Regional Development Fund (ERDF)/European Social Fund (ESF) "Cooperation in Applied Research between the University of Pardubice and Companies, in the Field of Positioning, Detection and Simulation Technology for Transport Systems (PosiTrans)" under Grant CZ.02.1.01/0.0/0.0/17_049/0008394. The Associate Editor coordinating the review process was Dr. Fabricio Guimaraes Baptista. *(Corresponding author: Lubos Rejfek.)*

Lubos Rejfek and Karel Juryca are with the Faculty of Electrical Engineering and Informatics (FEEI), University of Pardubice, 532 10 Pardubice, Czech Republic (e-mail: Lubos.Rejfek@upce.cz; karel.juryca@upce.cz).

Tan N. Nguyen is with Communication and Signal Processing Research Group, Faculty of Electrical and Electronics Engineering, Ton Duc Thang University, Ho Chi Minh City 729000, Vietnam (e-mail: nguyennhattan@tdtu.edu.vn).

Ladislav Beran is with ELDIS Pardubice, s.r.o., 533 01 Pardubice, Czech Republic (e-mail: ladislav.beran@eldis.cz).

Miroslav Voznak is with the Faculty of Electrical Engineering and Computer Science, VSB—Technical University of Ostrava, 708 00 Ostrava, Czech Republic (e-mail: miroslav.voznak@vsb.cz).

Digital Object Identifier 10.1109/TIM.2023.3279464

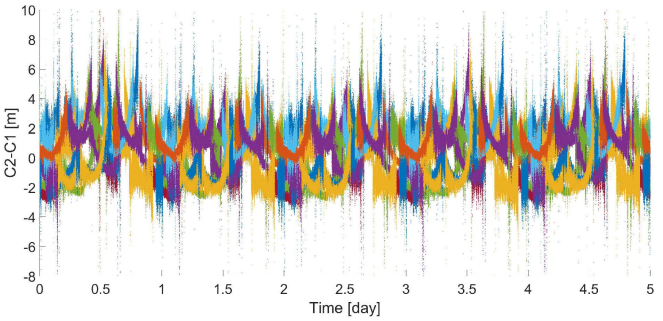

Fig. 2. Five-day interval showing the estimated pseudorange differences measured at the observatory Pardubice.

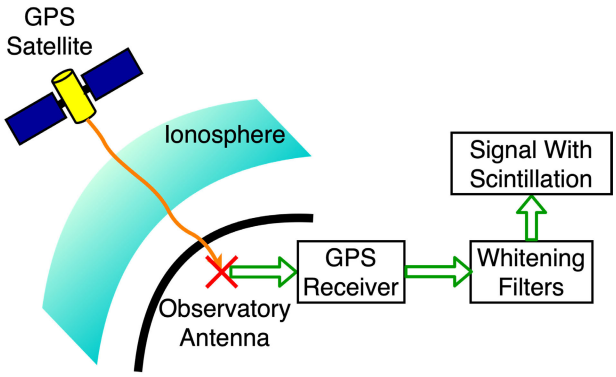

Fig. 3. Operating principle of the designed model.

signals. The TEC can be measured, for example, with the dual-frequency GNSS or it can be derived using the electron density profile obtained from the ionospheric radar. An example of the STEC received from one satellite is shown in [12]. The transformation of STEC to VTEC is described in [13]. The TEC can be calculated in different ways, for example, formula (2), according to [14]. Description of the signals transmitted by the GNSS is described in [15]. The quality of the on-board oscillators in GPS satellites is also important. Measurement and clock corrections are described in [16]

$$\mathrm{TEC} = \frac{1}{40.308} \cdot \frac{f_1^2 \cdot f_2^2}{f_1^2 - f_2^2} \cdot \left[L_1 \cdot \lambda_1 - L_2 \cdot \lambda_2 + K + nL \right] \tag{2}$$

where f_1 and f_2 are the frequencies of the satellite signals, L is the number of the phase rotations, and λ is wavelength and the indices 1 and 2 denote corresponding frequency bands.

The TEC maps created using many available GNSS receivers can be used for the description of the ionospheric variations, earthquakes, solar eclipses, solar flares, and monitoring of other events [14], [17]. The ionospheric scintillations produced by the small scales of ionospheric structures are other distortions of the phase and amplitude of the GNSS signals.

Fig. 2 shows the differences in pseudoranges between a specific GPS satellite (by color-coding) and the observatory. These pseudorange differences are obtained by using two different frequencies. The figure also shows that the delay is dependent on the local time and satellite zenith angle, i.e., the pseudorange difference is still not free of the slant effects. The pseudoranges are provided, e.g., in the RINEX format [18].

The dual-frequency concept does not routinely allow separation of the effect only on the specific frequency being used. We present a new approach using only a single frequency for the reconstruction of the TEC. By doing this, information about differences in the effects on both signals during propagation is still available.

Nevertheless, the downsides of this new approach are more difficult signal processing and dependence on the satellites' corrected orbital positions from NASA.

The GNSS signals include two types of errors: the system effects (caused by the technical parameters and must be suppressed), and the propagation effects (monitored parameters). The main task for signal processing is to suppress the system effects (distance of the satellite, time bias, and others). The system effects can be predicted, and the whitening filters are an appropriate approach for system error suppression. The system effect characteristics are then estimated, and the transient inversion function is applied to the measured data.

II. Description of Our Solution

We have created an algorithm using only one frequency for the measurement of ionospheric characteristics. To use this algorithm, two conditions must be fulfilled. First, to have adequately precise information about the satellite position in the required resolution. Second, the position of the GPS receiver antenna should be highly precise. If these conditions are met, we can apply the algorithm, which gives us information about the signal propagation delay. The time delay is dependent on the signal frequency and total electron concentration along the path (STEC). The first use of this algorithm is when we have just one frequency GPS receiver to obtain the data. The second possibility of using this algorithm is when we can get the scintillation for both frequencies separately and compare them. The current solution gives us only the mutual signal, and comparison is impossible. The current solution and our algorithm are compared in Section III.

A. Principle of the Proposed System

The operating principle of the designed model is shown in Fig. 3. The orange arrow represents the signal propagation from the satellite to the observatory (red cross). The exact distance between the observatory and the satellite can be obtained from (3). The errors in the measured distance obtained from the receiver are caused by the GNSS system (e.g., time bias) and by the ionosphere. These errors can be obtained as the difference between the real distance and the measured distance. As the first step, we need to estimate the receiver time bias. The receiver time bias is estimated by the GNSS receiver and saved in an sbf file. This knowledge will be used for the first whitening filter. The obtained signal still contains interferences and scintillations. The scintillations are too small compared to the interference, and the disturbed segments must be detected. The second filter is used for interference suppression. The whitening filters are described,

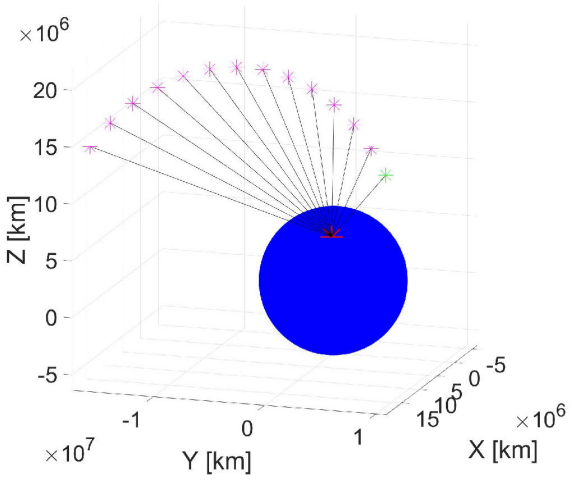

Fig. 4. Tracking of the GPS satellite G01 at the observatory Pardubice with the 15-min resolution. The red marker represents the observatory, magenta markers represent the historical satellite positions, and the green marker is the last satellite position.

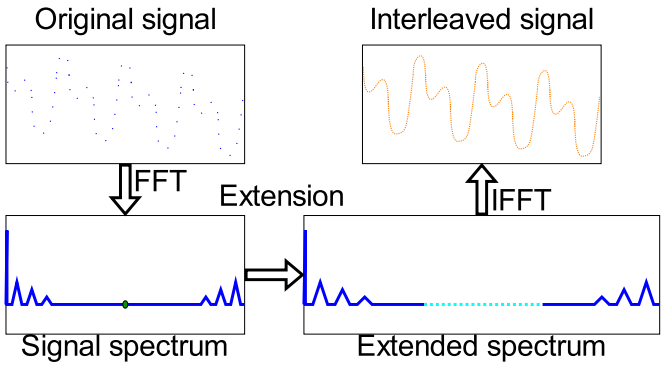

Fig. 5. Algorithm for the satellite distances timeline interleaving.

for example, in [20] and [21]

$$D = \sqrt{(X_S - X_O)^2 + (Y_S - Y_O)^2 + (Z_S - Z_O)^2} \quad (3)$$

where X, Y, and Z are the coordinates of the observatory (O) and the satellite (S).

B. Required Data and Their Post Processing

The satellite positions are obtained from the NASA website in sp3 format with 15-min resolutions [19]. In Fig. 4, the trajectory of a satellite (with the 15-min resolution) and the observatory position are shown. The black lines represent the distances in the recorded times. These distances are calculated using (3). Our algorithm uses these direct distances between the satellite and the observatory, but this resolution is not detailed enough for our purpose, and NASA's data must be interpolated.

The satellite positions can be interpolated by various methods, but the resulting interpolation error must be extremely small (much smaller than the expected results). We tested polynomial interpolation, but its error levels were higher than the scintillation signal. Therefore, we used the Zero Padding algorithm in a spectrum shown in Fig. 5. The first step is the transformation of the signal from the time domain

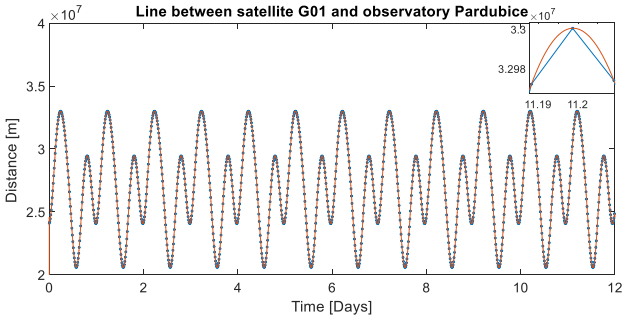

Fig. 6. Satellite (G01) distance measured from the Pardubice observatory (1 May 2021 to 12 May 2021) before interpolation (blue markers) and after the interpolation (orange line).

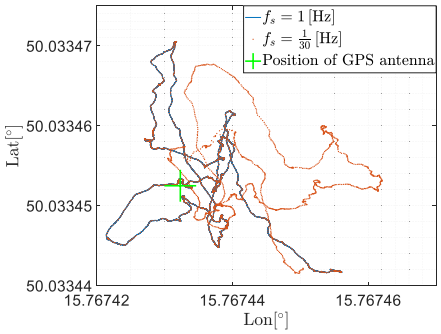

Fig. 7. Data from the measurements of the GPS antenna correct position. (Scale size of the graph is approximately 3 × 3 m in longitude and latitude).

(distances, between the satellite and the observatory, derived from the signal time delay) to the spectrum. The second step is the spectrum extension (by the middle value of the spectrum) to the required length. The third step is signal transformation back to the time domain. Application to the real positions is shown in Fig. 6. The blue dots represent the distances calculated from NASA's data, and the solid orange line represents the interleaved distances.

The antenna's position must be known with very high precision. The uncertainty in position must be much smaller than the distance error caused by expected scintillations. The calibrated position of the GPS antenna and data from the calibration measurement is shown in Fig. 7. The blue line represents data with a 1-s resolution, but the data in this resolution has a very big correlation. For this reason, we use data with a 30-s resolution (orange points in Fig. 7). The data are measured at two stations. The first is the reference station, where we know the exact position. The second is the antenna in the new position. Pseudoranges measured at the reference station give us information about the propagation delay and interferences for all used satellites and used frequencies. These corrections are applied to the data at the new station, and we can obtain (after the analysis of the set positions data) the corrected position (green cross in Fig. 7). The sequence of the positions must be recorded for at least 1 h and repeated 3 times with at least a 1-h break for suppression of the errors caused by the different positions of the antennas. The series of measured positions are used for the real position estimation (with a minor error). This position is used to calculate distances between the

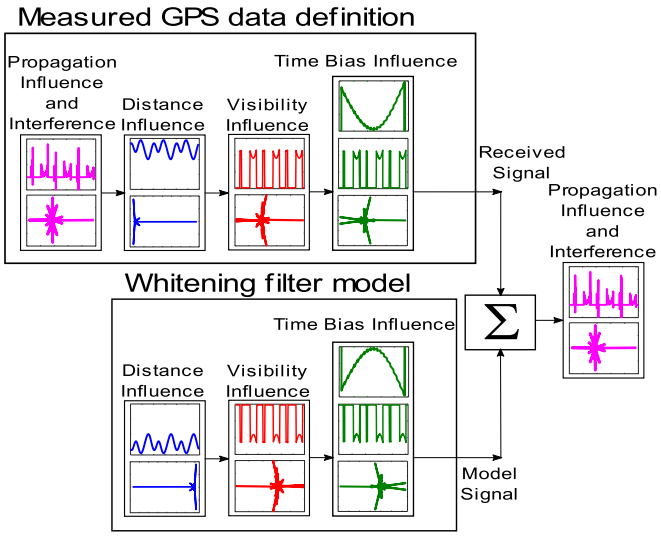

Fig. 8. Main whitening filter application, when the radio visibility, satellite distance, and receiver's time bias are suppressed.

satellites and the observatory (see (3), dimensions X, Y, and Z with the index O).

C. Whitening Filter Application

The first step for the signal processing is to create the whitening filter model. The whitening filter is used for the system effects suppression. This model has an inversion function of the expected undesirable influences on the received signal. The expected system effects are the real distances of the satellites, time bias of the receiver, satellite radio visibility, and interferences. The concept of the first whitening filter is shown in Fig. 8. The top block contains all expected influences, and the output is a real measured signal. The bottom block creates the whitening function for the real distance, time bias, and radio visibility suppression. The whitening filter creation is based on the measured data available from the NASA website (described above) and measurements from the GNSS receiver placed at the observatory (radio visibility of the satellite and time bias). The time bias ($\mathrm{TB}_{\mathrm{delay}}$) is recalculated to the propagation delay according to (4), where TB is the time bias in seconds and c_0 is the speed of light. The spectrum of the recorded signal is merged with the spectrum of the whitening filter output signal. The output signal contains only signal delay caused by signal propagation and interference. Examples of the signals generated in the parts of the whitening filter are in Fig. 9. The blue signal is the real satellite distance, and the green signal is the time bias. These signals are summed and multiplied by -1 to deduct it from the original signal. The red signal is the function of the radio visibility, and this signal is multiplied by the other two signals. The final model of the whitening filter (WS_k) is described by (5), where V_k is the satellite's radio visibility (1 if the signal is available and 0 if the satellite is not available), D_k is the distance for the sample k and TB_k is time bias for the sample k.

$$\mathrm{TB}_{\mathrm{delay}} = c_0 \cdot \mathrm{TB} \tag{4}$$

$$\mathrm{WS}_k = -V_k \cdot [D_k + \mathrm{TB}_k]. \tag{5}$$

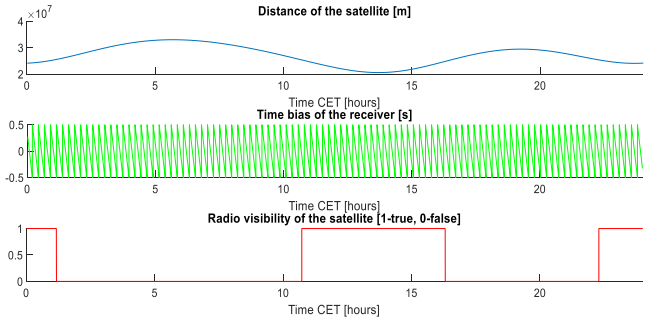

Fig. 9. Examples of the signals generated in the whitening filter blocks.

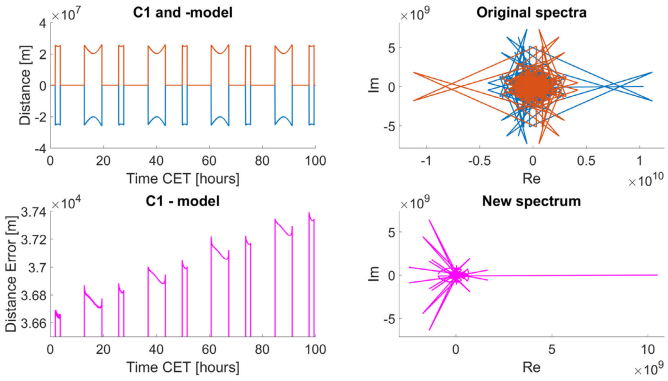

Fig. 10. Application of the whitening filter on the real data measured at the observatory Pardubice.

The application of the described whitening filter on the real data is shown in Fig. 10. The top part of the figure shows the received signal (blue curve) and the output signal from the whitening filter model (red curve) in time and spectral domains. The bottom part of the figure shows the signal after the whitening filter application in those domains. We can see that the distance errors are different in every observation because the satellite's orbital period is different from the earth's rotation period. The rest of our algorithm uses only separated observations.

D. Detection and Suppression of the GPS Interference

Fig. 11 shows the distance error caused by the propagation delay and GPS interference (signal drawn by the magenta color). The interference is observed as periodic changes in the distance error (see Fig. 11). The interference is zoomed in for a better illustration. The interference causes deviation from the main trend and is probably created by the signal modulation and can be removed. The periodicity of the interference with the rectangular envelope and linear sweeping suggests that the interference is industrial. The signal delay changes cause this interference. The sources of this interference can be only two: the time sweeping in the receiver (decreasing of the precision by the GPS receiver is not probable), and the keying created by the satellite operator (it is a more probable case than the previous one because the operator can have the key for the interference suppression for their purpose). Because the exact modulation keying is unavailable, the algorithm must detect interference intervals based on the interference characteristics.

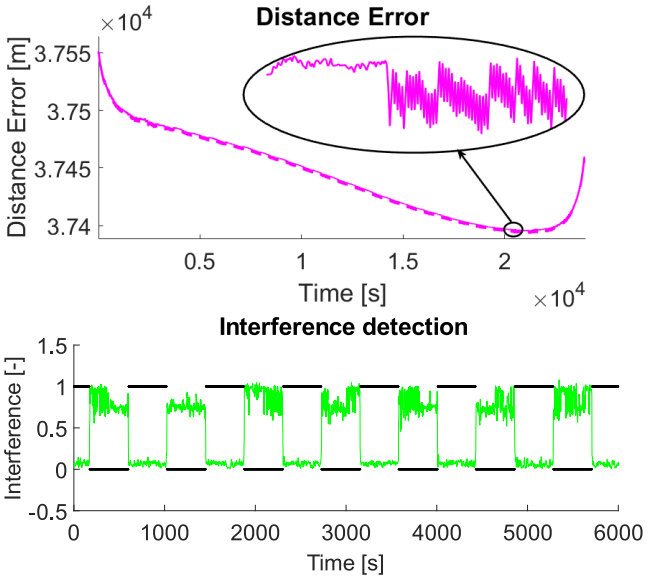

Fig. 11. Example of the input data for the algorithm (top graph) and detected interfered segments (bottom graph).

TABLE I
FILTERS' PARAMETERS

FILTER	PARAMETER	VALUE	UNIT
LPR	REMOVED SPECTRAL COMPONENTS	20	%
HPR	MEDIAN WINDOW LENGTH	5	NO

The interference envelope has a higher frequency than the other trends, and the 20% low frequencies were removed from the spectrum. The spectrum of the signal is calculated by the Fast Fourier Transform—(6) (see [22]). The next step is interference modulation suppression. The removal of the high frequencies created by the interference modulation is given by (8) after the signal is transformed back to the time domain by the inverse fast Fourier transform (IFFT) function [see (7)]. The thresholding must be applied on the green signal (d), and the threshold value is 50% of the whole signal median. We must apply video detection because false alerts can be created. The video detection removes all alerts shorter than the set minimal duration. The output signal is shown in Fig. 11 using black color. The zero values represent interference intervals. The filters' parameters are described in Table I

$$S[k] = \sum_{n=0}^{N-1} s(n) e^{-j\frac{2\pi nk}{N}} \tag{6}$$

$$s_f[k] = \frac{1}{N} \sum_{n=0}^{N-1} S_f(k) e^{j\frac{2\pi nk}{N}} \tag{7}$$

$$d[n] = \tilde{s} = \mathrm{Me}_{n+\frac{L}{2}}^{n-\frac{L}{2}}(s_f[n]) \tag{8}$$

where s is the signal sample in the time domain, d is the demodulated interference envelope, L is the window length, and Me is the median function.

The intervals with interference and without interference are separated as the output from the previous algorithm. The segments without interference can be used to calculate the smoothed delay of the signal propagation without interference

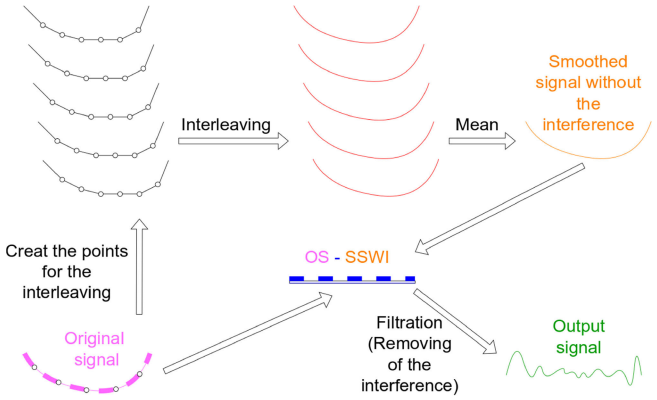

Fig. 12. Algorithm for the signal with scintillation extraction.

and for the scintillation estimation. The algorithm for this processing is in Fig. 12. New signals (gray curves) are created from the segments without interference. The first gray signal takes the first points in these segments, the second one takes the second point, and so on. These signals, with a smaller sampling frequency, are interleaved (red curves). Because of the choice of the samples, the new signals are shifted (red curve). These new signals must be shifted back to the original position. We can compute the average signal (orange curves, Fig. 12) when the time shift is suppressed. This is used for the suppression of the scintillation influences. The new smoothed signal can be our output if our target is to obtain the main propagation delay. The difference between the original signal (magenta curve) and smoothed signal gives us the scintillation signal with the interference (blue curve). Because we know when the signal is disturbed, we can use demodulation on these segments, which gives us a modulation envelope. The filter can realize the demodulation, and after the demodulation of all segments, we will get the scintillations in time (green curve, Fig. 12). The application of this algorithm on the real signal is shown in Fig. 13. The curve colors in Fig. 13 correspond to the colors used in the algorithm description. We can see significant errors in the signal interleaving, very close to the edges of the signal. In the main part of the signal, the errors are negligible. The output signal is compared with the signal obtained by the dual-frequency approach (black curve).

III. RESULTS EVALUATION

The results from our algorithm are compared with the signal obtained by the classical dual-frequency approach. The existing correlation is shown in Figs. 14–16, where green represents signals derived by our algorithm. The black curve represents the signals obtained as P2–P1. The signals in the global perspective (left panels of Figs. 14–16) do not look very similar. This is caused by the scaling of the figures. If the zoom is applied (the right panels), we can see that the scintillations are very similar. The red line indicates the segments where the interference was removed.

Fig. 17 shows three examples of how the pseudoranges P2 and P1 affect the final signal. Case "A" is highlighted in Fig. 18. This represents the effect when the signal from P1 is approximately constant, and the signal deviation is

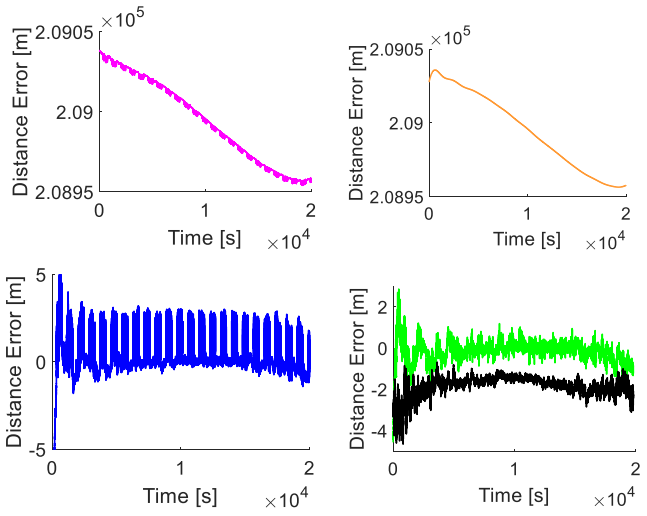

Fig. 13. Input signal for the algorithm which extracts the scintillations (left top), the interpolated signal (right-top), signal with the scintillations and interferences (left bottom) and after the interference suppression (green signal in the right bottom, the black signal is obtained as the difference of the pseudoranges P2–P1).

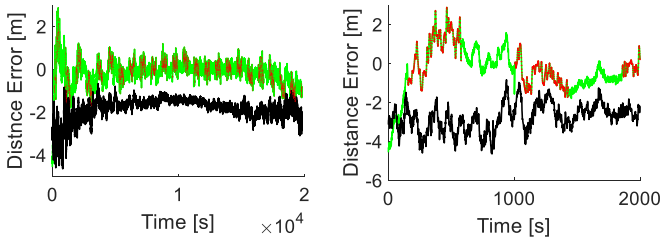

Fig. 14. One observation of GPS satellite G01 and zoom on the part of this observation (6 May 2021).

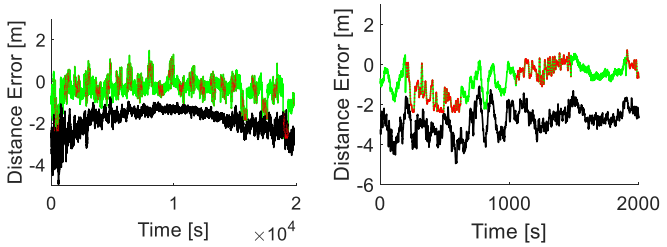

Fig. 15. One observation of GPS satellite G01 and zoom on the part of this observation (5 May 2021).

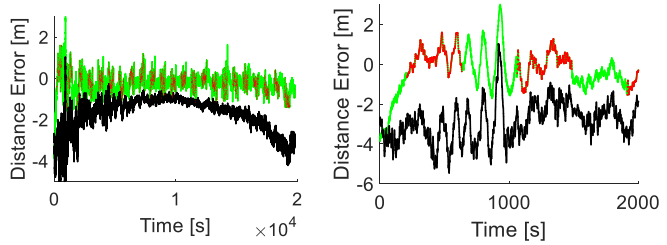

Fig. 16. One observation of GPS satellite G27 and zoom on the part of this observation (6 May 2021).

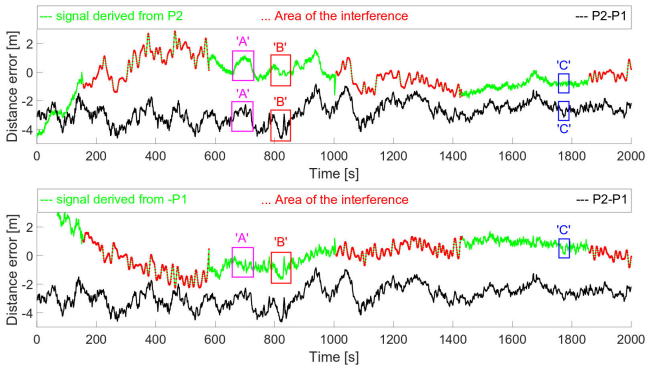

Fig. 17. Selection of the cases which can happen in the classical processing.

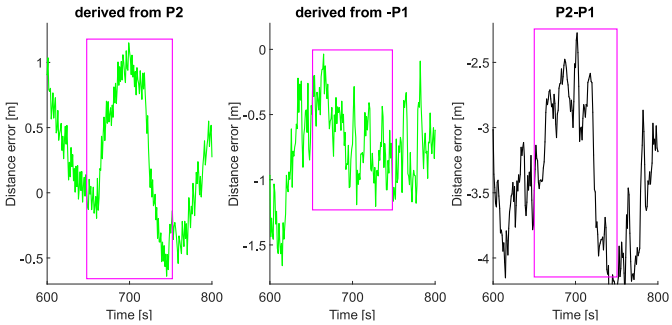

Fig. 18. Case "A" from Fig. 17, the event created just by the effects on the pseudorange obtained from frequency 2.

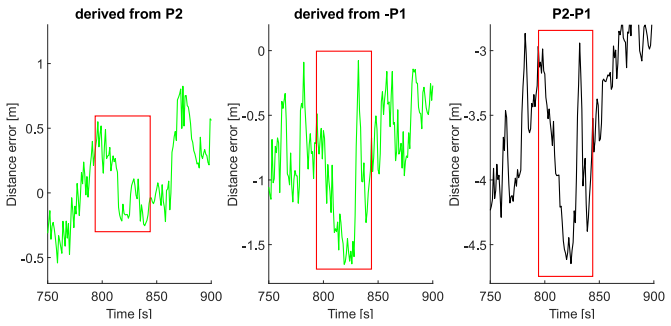

Fig. 19. Case "B" from Fig. 17, the event created as a combination of the effects on the pseudorange obtained from both used GPS frequencies.

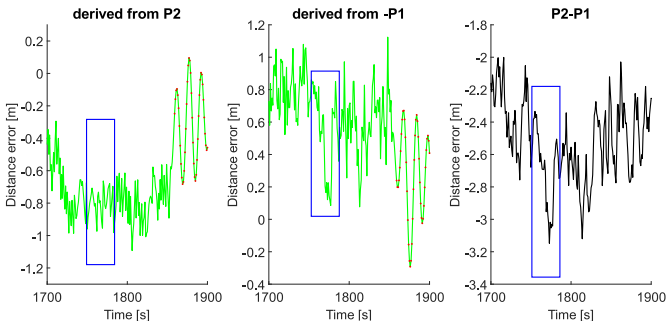

Fig. 20. Case "C" from Fig. 17, the event created just by the effects on the pseudorange obtained from frequency 1.

caused just by the pseudorange P2. Case "B" is highlighted in Fig. 19. In this case, we can see that both pseudoranges affect the final signal obtained by the classical dual-frequency approach. Case "C" shows the example when the signal from the pseudorange P2 is constant. The signal obtained by the classical approach can also contain only a contribution from the P1 signal (see Fig. 20).

TABLE II
DATA USED FOR THE ALGORITHM TEST

PARAMETER	VALUES	UNITS	NOTES
DATA RECORD DURATION	12	DAYS	NO
SAMPLING FREQUENCY	1	HZ	NO
OBSERVATIONS NUMBER	24	CYCLES	NO
MONITORED SATELLITES	31	NO	SATELLITE NO. 23 OUT OF SERVICE DURING MEASUREMENT

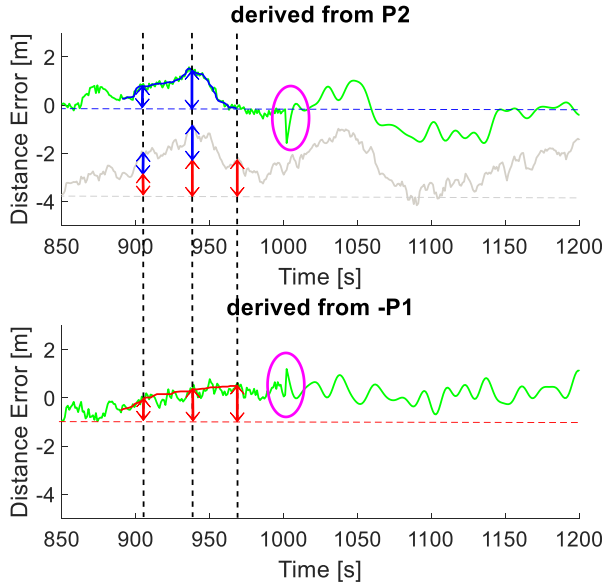

Fig. 21. Analysis of the signal obtained as the difference of pseudoranges and influence of used pseudoranges on the created signal.

A detailed description of the effects of both pseudoranges on the merged signal is shown in Fig. 21. The blue marked signal is derived by our algorithm using pseudorange P2, and the red one using pseudorange P1. We can see that the influence of the signal from P1 fluently increases during the monitored interval, but the influence of the signal from P2 increases and decreases during the monitored interval. It shows the benefit of the proposed algorithm, where an operator can compare the signal propagation influences to every carrier wave separately. This figure also shows us the disadvantages of our algorithm when the signal from the interfered part does not contain higher frequencies (fast effects). The problem with the connections of the signals (interfered and non-interfered) around time 1000 s is denoted by magenta. Both described problems are in the defined areas, and we can easily exclude these regions if it is unacceptable for our purposes. If we exclude these parts, we will have no information about the propagation channel during these excluded times. The parameters of the measurements realized for the test of the algorithm are described in Table II. Data presented in this article were selected from this measurement and used to compare the proposed approach with the classical dual-frequency approach.

IV. CONCLUSION

A new algorithm, which can be used for GPS signal post-processing is presented. The post-processed signals can be used for future research and help us monitor the ionospheric responses to several disturbances such as earthquakes, increases in solar X-rays, strong geomagnetic storms, etc.

The benefits of our algorithm are two. The first benefit is that a single-frequency GPS receiver is satisfactory for ionospheric monitoring. The second and more important benefit is that we can study the effects on all available frequencies separately if we have a GPS receiver that can receive more frequencies (bands L1, L2, and L5). The disadvantage of our algorithm is more complex signal processing. We must meet specific conditions (for example, a precisely measured position of the GPS receiver antenna). During the disturbed intervals, the information about the fast events is lost and cannot be recovered.

The results described in the article show that the classically processed signal (P2–P1) merges the effects from both frequencies, and we cannot separate them later. Our algorithm does not merge these effects, as shown in the results part of the article. Consequently, we can better understand processes in the ionosphere.

Our algorithms still have a few limitations. The demodulation of the interference removes fast events, and the other events are described by their trends only. Interference affects the signals with an alternation of 50% and can easily detect if the current signal part is affected. The second problem is the connection between the disturbed and non-disturbed parts. These effects are the inspiration for following research to improve these deficiencies. In the next step, we plan to use neural networks for data post-processing.

ACKNOWLEDGMENT

The author would like to thank Charles Hooper for the proofreading.

REFERENCES

[1] M. J. Kalaee and Y. Katoh, "Plasma frequency demand for mode conversion processes from slow Z-mode to LO-mode waves in an inhomogeneous plasma," *Earth, Planets Space*, vol. 72, no. 1, pp. 1–7, Dec. 2020.

[2] F. F. Chen, *Introduction to Plasma Physics*. New York, NY, USA: Plenum Press, 1974.

[3] Z. Mosna et al., "Ionospheric storm of September 2017 observed at ionospheric station pruhonice, the Czech republic," *Adv. Space Res.*, vol. 65, no. 1, pp. 115–128, Jan. 2020.

[4] B. W. Reinisch et al., "New digisonde for research and monitoring applications," *Radio Sci.*, vol. 44, no. 1, pp. 1–15, Feb. 2009, doi: 10.1029/2008RS004115. [Online]. Available: http://ieeexplore.ieee.org/stamp/stamp.jsp?tp=&arumber=7775865&isnumber=7771653

[5] T. Verhulst et al., "Vertical and oblique HF sounding with a network of synchronised ionosondes," *Adv. Space Res.*, vol. 60, no. 8, pp. 1644–1656, Oct. 2017.

[6] T. G. W. Verhulst et al., "Improving signal-to-noise ratio in oblique ionosonde soundings using new hardware capability of the DPS4D ionosonde," in *Proc. 2nd URSI Atlantic Radio Sci. Meeting (AT-RASC)*, May 2018, p. 1. [Online]. Available: https://ieeexplore.ieee.org/document/8471393

[7] K. Nozaki, "FMCW lonosonde for the SEALION project," *J. Nat. Inst. Inf. Commun. Technol.*, vol. 56, nos. 1–4, pp. 287–298, 2009.

[8] J. Chum et al., "Continuous Doppler sounding of the ionosphere during solar flares," *Earth, Planets Space*, vol. 70, no. 1, pp. 1–19, Dec. 2018.

[9] T. Sindelarova et al., "Solar eclipse effects in the ionosphere observed by continuous Doppler sounding," *Adv. Space Res.*, vol. 62, no. 4, pp. 785–800, Aug. 2018.

[10] J. C. Uwamahoro, J. B. Habarulema, and D. Buresova, "Highlights about the performances of storm-time TEC modelling techniques for low/equatorial and mid-latitude locations," *Adv. Space Res.*, vol. 63, no. 10, pp. 3102–3118, May 2019.

[11] G. S. Bust and C. N. Mitchell, "History, current state, and future directions of ionospheric imaging," *Rev. Geophys.*, vol. 46, no. 1, pp. 1–23, 2008. [Online]. Available: https://agupubs.onlinelibrary.wiley.com/doi/epdf/10.1029/2006RG000212

[12] S. D. Yenen, F. Arikan, and T. Gulyaeva, "Comparison of IRI-Plas STEC and IONOLAB-STEC over a midlatitude GPS network," in *Proc. 9th Int. Conf. Recent Adv. Space Technol. (RAST)*, Jun. 2019, pp. 649–653.

[13] D. Okoh et al., "A regional GNSS-VTEC model over Nigeria using neural networks: A novel approach," *Geodesy Geodynamics*, vol. 7, no. 1, pp. 19–31, Jan. 2016.

[14] E. L. Afraimovich et al., "A review of GPS/GLONASS studies of the ionospheric response to natural and anthropogenic processes and phenomena," *J. Space Weather Space Climate*, vol. 3, p. 27, 2013.

[15] R. Xi, Q. He, and X. Meng, "Bridge monitoring using multi-GNSS observations with high cutoff elevations: A case study," *Measurement*, vol. 168, Jan. 2021, Art. no. 108303.

[16] K. Maciuk, J. Kudrys, B. Skorupa, and Z. Malkin, "Testing the product quality of Galileo and GPS on-board oscillators," *Measurement*, vol. 167, Jan. 2021, Art. no. 108261.

[17] S. Jin, R. Jin, and D. Li, "GPS detection of ionospheric Rayleigh wave and its source following the 2012 Haida Gwaii earthquake," *J. Geophys. Res., Space Phys.*, vol. 122, no. 1, pp. 1360–1372, Jan. 2017.

[18] W. Gurtner and L. Estey, *RINEX: The Receiver Independent Exchange Format Version 2.11*, document RTCA DO 229, Astronomical Institute University of Berne, UNAVCO, Boulder, CO, USA, 2012.

[19] S. Hilla, "The extended standard product 3 orbit format (SP3-c)," Nat. Geodetic Surv. Nat. Ocean Service, NOAA, Silver Spring, MD, USA, Tech. Rep., 2010.

[20] A. Arienzo, F. Argenti, L. Alparone, and M. Gherardelli, "Accurate despeckling and estimation of polarimetric features by means of a spatial decorrelation of the noise in complex PolSAR data," *Remote Sens.*, vol. 12, no. 2, p. 331, Jan. 2020.

[21] J. Jinsoo. (2021). *Real-Time Noise Cancelling Approach on Innovations-Based Whitening Application to Adaptive FIR RLS in Beamforming Structure*. Adaptive Filtering, Lino Garcia. [Online]. Available: https://www.intechopen.com/books/adaptive-filtering/real-time-noise-cancelling-approach-on-innovations-based-whitening-application-to-adaptive-fir-rls-i/

[22] M. Inci, M. Buyuk, A. Tan, K. C. Bayindir, and M. Tumay, "Multipurpose compensation scheme for voltage sag/swell and selective harmonics elimination in distribution systems," *Adv. Electr. Electron. Eng.*, vol. 16, no. 1, pp. 71–80, Apr. 2018.

Lubos Rejfek was born in Chrudim, Czechoslovakia, in 1985. He received the Ph.D. degree from the Faculty of Electrical Engineering and Informatics, University of Pardubice, Pardubice, Czech Republic, in 2017.

He is currently a Lecturer at the Faculty of Electrical Engineering and Informatics, University of Pardubice, and is also employed at the IAP CAS, Beijing, China.

Karel Juryca (Member, IEEE) received the master's degree from the Faculty of Electrical Engineering and Informatics, University of Pardubice, Pardubice, Czech Republic, in 2016.

He has been a Lecturer at the Faculty of Electrical Engineering and Informatics, University of Pardubice, since 2019. His topic are radars and communication systems.

Tan N. Nguyen (Member, IEEE) was born in Nha Trang City, Vietnam, in 1986. He received the B.S. degree in electronics from the Ho Chi Minh University of Natural Sciences, Ho Chi Minh City, Vietnam, in 2008, the M.S. degree in telecommunications engineering from Vietnam National University, Ho Chi Minh City, in 2012, and the Ph.D. degree in communications technologies from the Faculty of Electrical Engineering and Computer Science at VSB—Technical University of Ostrava, Ostrava, Czech Republic, in 2019.

He joined the Faculty of Electrical and Electronics Engineering of Ton Duc Thang University, Ho Chi Minh City, in 2013, and since then has been lecturing. He is with the Communication and Signal Processing Research Group, Faculty of Electrical and Electronics Engineering, Ton Duc Thang University. His major interests are cooperative communications, cognitive radio, physical layer security, and signal processing.

Ladislav Beran was born in Pardubice, Czechoslovakia, in 1989. He received the Ph.D. degree from the Faculty of Electrical Engineering and Informatics, University of Pardubice, Pardubice, Czech Republic, in 2022.

He is currently working at Eldis Pardubice, s.r.o., Pardubice. His topics are neural networks and their implementation in the navigation of robotics platforms.

Miroslav Voznak (Senior Member, IEEE) received the Ph.D. degree in telecommunications from the Faculty of Electrical Engineering and Computer Science, VSB—Technical University of Ostrava, Ostrava, Czech Republic, in 2002, and the Habilitation degree from the VSB—Technical University of Ostrava, in 2009.

He was appointed as a Full Professor in electronics and communications technologies at the VSB—Technical University of Ostrava, in 2017.